*Nano Research* 2016, 9(8): 2445–2457
DOI 10.1007/s12274-016-1130-x
**Research Article**
ISSN 1998-0124
CN 11-5974/O4

# Interface-modulated approach toward multilevel metal oxide nanotubes for lithium-ion batteries and oxygen reduction reaction

Jiashen Meng[1,§], Chaojiang Niu[1,§], Xiong Liu[1], Ziang Liu[1], Hongliang Chen[2], Xuanpeng Wang[1], Jiantao Li[1], Wei Chen[1], Xuefeng Guo[2] (✉), and Liqiang Mai[1] (✉)

[1] *State Key Laboratory of Advanced Technology for Materials Synthesis and Processing, Wuhan University of Technology, Wuhan 430070, China*
[2] *Center for Nanochemistry, Beijing National Laboratory for Molecular Sciences, State Key Laboratory for Structural Chemistry of Unstable and Stable Species, College of Chemistry and Molecular Engineering, Peking University, Beijing 100871, China*
[§] *These authors contributed equally to this work.*

**Received:** 27 March 2016
**Revised:** 28 April 2016
**Accepted:** 3 May 2016



**KEYWORDS**
interface-modulated approach,
multilevel nanotubes,
metal oxide,
lithium-ion battery (LIB),
oxygen reduction reaction (ORR)

## ABSTRACT

Metal oxide hollow structures with multilevel interiors are of great interest for potential applications such as catalysis, chemical sensing, drug delivery, and energy storage. However, the controlled synthesis of multilevel nanotubes remains a great challenge. Here we develop a facile interface-modulated approach toward the synthesis of complex metal oxide multilevel nanotubes with tunable interior structures through electrospinning followed by controlled heat treatment. This versatile strategy can be effectively applied to fabricate wire-in-tube and tube-in-tube nanotubes of various metal oxides. These multilevel nanotubes possess a large specific surface area, fast mass transport, good strain accommodation, and high packing density, which are advantageous for lithium-ion batteries (LIBs) and the oxygen reduction reaction (ORR). Specifically, shrinkable $CoMn_2O_4$ tube-in-tube nanotubes as a lithium-ion battery anode deliver a high discharge capacity of ~565 mAh·g$^{-1}$ at a high rate of 2 A·g$^{-1}$, maintaining 89% of the latter after 500 cycles. Further, as an oxygen reduction reaction catalyst, these nanotubes also exhibit excellent stability with about 92% current retention after 30,000 s, which is higher than that of commercial Pt/C (81%). Therefore, this feasible method may push the rapid development of one-dimensional (1D) nanomaterials. These multifunctional nanotubes have great potential in many frontier fields.

## 1 Introduction

Because of their unique properties, hollow structures have been widely applied for catalysis, chemical sensing, drug delivery, and energy storage [1–12]. Hollow structures have experienced a structural

Address correspondence to Liqiang Mai, mlq518@whut.edu.cn; Xuefeng Guo, guoxf@pku.edu.cn

evolution from simple to complex during recent decades [13]. Compared with simple hollow structures, complex multilevel hollow structures show multilevel interior spaces and multiphase interfaces, which may change the physicochemical properties and enable many potential applications [14–19]. However, it is difficult to efficiently synthesize these multilevel hollow structures. Therefore, the development of a general synthesis strategy for multilevel hollow structures with a desirable composition and delicate morphology is challenging for both fundamental studies and practical applications.

Intensive efforts have been made to synthesize multilevel metal oxide hollow structures. Lou et al. obtained double-shelled $SnO_2$ hollow spheres and "nanococoons" by shell-by-shell deposition of $SnO_2$ on spherical and nonspherical silica [20, 21]. Dong et al. reported the synthesis of multishelled ZnO hollow microspheres by thermal decomposition of carbonaceous microspheres with adsorbed zinc ions [22]. The optimized sample has a large surface area and can reflect and scatter light, leading to a high energy conversion efficiency in dye-sensitized solar cells. Zhou et al. synthesized double-shelled $CoMn_2O_4$ hollow microcubes with enhanced lithium-ion battery (LIB) performance via a facile coprecipitation and subsequent annealing method [23]. Despite these great successes, an efficient strategy for general synthesis of one-dimensional (1D) multilevel hollow structures has seldom been reported owing to the anisotropic features and complex construction process [24–34].

Metal oxides, especially ternary transition metal oxides, are remarkably attractive candidates for use as LIB anodes and electrocatalysts owing to their low cost and high electrochemical activity [35–42]. However, the large volume variation is a major and catastrophic problem in LIBs. It leads to serious pulverization and aggregation, resulting in structural degradation and, eventually, in rapid capacity fading [43]. However, hollow structures overcome this problem by buffering the large volume change. Nevertheless, owing to their low packing density, hollow structures suffer from a relatively low volumetric energy, which still limits their practical application [44, 45]. On the other hand, multivalent metal spinels, especially $Co_{3-x}Mn_xO_4$, are considered to be attractive nonprecious oxygen electrocatalysts [46–48]. Their electrocatalytic processes are strongly related to the number of available active sites [49]. Generally, these spinels are synthesized through traditional ceramic methods, which seriously limit their electrochemical properties because of the large particle size and low surface area [46].

Herein, we report a facile and versatile interface-modulated method of synthesizing multilevel metal oxide nanotubes with tunable interior structures. By controlling the polymer/metal oxide interface, solid electrospun nanofibers can be converted into shrinkable wire-in-tube and tube-in-tube nanotubes (Fig. 1). In this regard, it is highly desirable to design and obtain multilevel metal oxides with various compositions. Specifically, the synthesized shrinkable $CoMn_2O_4$ tube-in-tube nanotubes exhibit excellent electrochemical performance in LIBs and the oxygen reduction reaction (ORR).

## 2 Experimental

### 2.1 Materials synthesis

#### *2.1.1 Preparation of shrinkable metal oxide wire-in-tube nanotubes*

The preparation of shrinkable $CoMn_2O_4$ wire-in-tube nanotubes is presented as an example. First, low-molecular-weight (98%–99% hydrolyzed), medium-molecular-weight (86%–89% hydrolyzed), and high-molecular-weight (98%–99% hydrolyzed) polyvinyl alcohol (PVA) in a weight ratio of 3:2:1 (9.5 wt.%) were dissolved in 20 mL of deionized water. 1.5 mmol $Co(CH_3COO)_2{\cdot}4H_2O$ and 3 mmol $Mn(CH_3COO)_2{\cdot}4H_2O$ were added to the prepared PVA precursor. After the mixture was stirred at 80 °C for 5 h, a viscous, uniform, transparent solution was obtained. Subsequently, the precursor solution was electrospun (SS-2534H, UCALERY Co., Beijing, China) at a constant flow rate and a high voltage of 12 kV. The composite nanowires were collected on revolving aluminum foil. After drying at 80 °C for 12 h, the composite nanowires were heated to 280 °C at 10 °C·min$^{-1}$ and held at 280 °C for 1 h in air. Then, the primary product was heated to 500 °C at 1 °C·min$^{-1}$ and kept at that temperature for 3 h in air. Shrinkable $CoMn_2O_4$ wire-in-tube nanotubes were obtained. Shrinkable wire-in-tube nanotubes

of other metal oxides were synthesized by a similar process.

*2.1.2 Preparation of shrinkable metal oxide tube-in-tube nanotubes*

The preparation of shrinkable $CoMn_2O_4$ tube-in-tube nanotubes is presented as an example. Electrospun nanofibers were obtained by the processes described above. After drying at 80 ℃ for 12 h, the composite nanowires were heated to 280 ℃ at 1 ℃·min$^{-1}$ and held at 280 ℃ for 1 h in air. Then, the primary product was heated to 500 ℃ at 10 ℃·min$^{-1}$ and kept at that temperature for 3 h in air. Shrinkable $CoMn_2O_4$ tube-in-tube nanotubes were obtained. Shrinkable tube-in-tube nanotubes of other metal oxides were synthesized by a similar process.

## 2.2 Characterization

The crystallographic characteristics of the final products were measured using a Bruker D8 Discover X-ray diffractometer equipped with a Cu K$\alpha$ radiation source; the samples were scanned over a 2$\theta$ range of 10° to 80° at room temperature. Scanning electron microscopy (SEM) images were collected using a JEOL-7100F scanning electron microscope, and transmission electron microscopy (TEM) images were collected using a JEM-2100F transmission electron microscope. The Brunauer–Emmett–Teller (BET) surface area was calculated from nitrogen adsorption isotherms measured at 77 K using a Tristar-3020 instrument.

## 2.3 Electrochemical measurements

For the lithium-ion battery, 2,016 coin cells were assembled in a glovebox filled with pure argon gas. Lithium foil was used as the anode, and a solution of $LiPF_6$ (1 M) in ethylene carbonate/diethyl carbonate (1:1 v/v) was used as the electrolyte. The cathode was composed of a ground mixture of 70% active material, 25% acetylene black, and 5% graphene oxides (graphene oxides were synthesized through a modified Hummers' method). After coating onto copper foil, the electrode film was uniformly cut into round slices ~0.5 cm$^2$ in area weighing a total of ~1.2 mg; the corresponding areal mass loading was 2.4 mg·cm$^{-2}$. Galvanostatic charge–discharge measurements were performed using a multichannel battery testing system (LAND CT2001A). Cyclic voltammograms (CVs) and electrochemical impedance spectra were collected at room temperature using an Autolab potentiostat/galvanostat.

For the oxygen reduction reaction, the electrocatalytic activities of shrinkable $CoMn_2O_4$ tube-in-tube nanostructure catalysts toward ORR were measured in $O_2$-saturated 0.1 M KOH aqueous solution, with a saturated calomel reference electrode (SCE), a Pt wire counter electrode, and a working electrode. An ink of the catalyst was prepared by mixing 5 mg of catalyst powder and 5 mg of Vulcan XC72R (VXC72R) with 50 μL of a 5 wt.% Nafion solution, 200 μL of deionized water, and 750 μL of isopropanol, and placing the resulting mixture in an ultrasonic bath. CVs at a sweep rate of 5 mV·s$^{-1}$ were recorded in the potential range of 0.1 to −0.8 V versus SCE. Linear sweep voltammetry (LSV) was performed in $O_2$-saturated 0.1 M KOH. ORR polarization curves were recorded at a scan rate of 5 mV·s$^{-1}$ under various electrode rotation rates (400, 625, 900, 1,225, and 1,600 rpm). The Pt ring potential was set at 0.5 V versus SCE to monitor the formation of peroxide species. All the potentials were transferred to the reversible hydrogen electrode potential scale.

Before each measurement, 0.1 M KOH electrolyte was bubbled with $O_2$ for more than 30 min. Rotating ring-disk electrode (RRDE) measurements were performed at 1,600 rpm using a CHI 760 E electrochemical workstation with an RRDE-E7R9 rotator (Pine Co., Ltd.).

The ORR kinetics was analyzed using the Koutecky–Levich (K–L) equation [49]

$$\frac{1}{i}=\frac{1}{i_k}+\frac{1}{i_d}=-\frac{1}{nFAkC^0}-\frac{1}{0.62nFAD_{O_2}^{2/3}\upsilon^{-1/6}C^0\omega^{1/2}} \quad (1)$$

where $i$, $i_k$, and $i_d$ correspond to the measured, kinetic, and diffusion-limiting current, respectively; $n$ is the overall transferred electron number; $F$ is the Faraday constant; $A$ is the geometric electrode area (cm$^2$); $k$ is the rate constant for oxygen reduction; $C^0$ is the saturated concentration of oxygen in 0.1 M KOH; $D_{O_2}$ is the diffusion coefficient of oxygen; $\upsilon$ is the kinetic viscosity of the solution; and $\omega$ is the rotation rate

(rad·s$^{-1}$) of the electrode. Further, the percentage of peroxide species ($HO_2^-$) with respect to the total generated oxygen reduction products and the electron reduction number ($n$) were calculated as

$$HO_2^- = 200\frac{I_r / N}{I_d + I_r / N} \quad (2)$$

$$n = 4\frac{I_d}{I_d + I_r / N} \quad (3)$$

where $I_d$ is the disk current, $I_r$ is the ring current, and $N$ is the current collection efficiency (0.37) of the RRDE.

## 3 Results and discussion

### 3.1 Controlled interface-modulated mechanism

In the initial stage, low-, medium-, and high-molecular-weight PVA are dissolved in deionized water with moderate inorganic salts (denoted as S in Fig. 1), forming a homogeneous precursor solution (Table S1 in the ESM). As we reported previously, the PVAs with different molecular weights tend to separate into three layers instead of mixing together under the strong electrostatic tension force [50]. As a result, the inorganic salts are uniformly dispersed in coaxial nanofibers after electrospinning (Fig. 1 and Fig. S1 in the ESM). According to the thermogravimetric (TG) curves, low-, medium-, and high-molecular-weight PVA successively pyrolyze as the temperature increases (Fig. S2 in the ESM). Therefore, the pyrolysis direction of composite nanofibers is from the center to the outside, which is different from the traditional pyrolysis direction (from the outside to the center) [6, 23, 30]. In the subsequent heat treatments, two opposite forces exist in the electrospun fibers, namely, the contraction force ($F_c$) due to pyrolysis of PVA and the adhesive force ($F_a$) from the outer shell. During the heat treatment, the temperature gradient determines the strength of $F_c$ and $F_a$, and thus the radial interface-contract direction.

When electrospun nanofibers are sintered to 280 ˚C at a high heating rate of 10 ˚C·min$^{-1}$ in air, $F_c$ exceeds

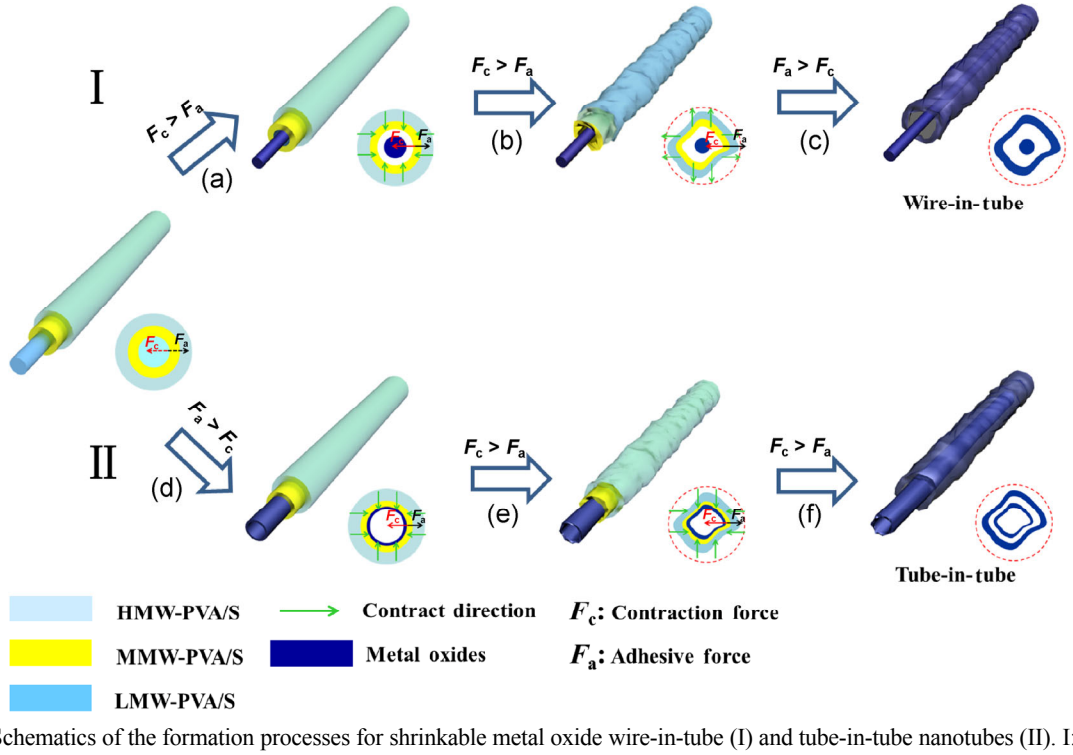


**Figure 1** Schematics of the formation processes for shrinkable metal oxide wire-in-tube (I) and tube-in-tube nanotubes (II). I: Electrospun nanofibers are (a) heated to low temperature (280 ˚C, 10 ˚C·min$^{-1}$) and (b) held at 280 ˚C for 1 h in air; then (c) the sample is annealed at high temperature for 3 h in air (500 ˚C, 1 ˚C·min$^{-1}$). II: Electrospun nanofibers are (d) heated to low temperature (280 ˚C, 1 ˚C·min$^{-1}$), (e) held at 280 ˚C for 1 h in air, and (f) finally sintered for 3 h in air (500 ˚C, 10 ˚C·min$^{-1}$).

$F_a$ (Fig. 1(a) and Fig. S3(a) in the ESM). The inner low-molecular-weight PVA decomposes rapidly and contracts inward along with the inorganic salts, forming wire-in-tube nanotubes (Fig. 1(b) and Fig. S4(b) in the ESM). Then, when the sample is sintered at 280 °C for 1 h, the outer nanotubes tend to shrink inward owing to the softness of the outer polymer shells (Fig. 1(c) and Fig. S4(c) in the ESM) [51]. Subsequently, as the product is heated to 500 °C at 1 °C·min$^{-1}$ for 3 h, shrinkable composite nanotubes slowly pyrolyze, forming outer inorganic shells, because $F_c$ is smaller than $F_a$. Finally, shrinkable wire-in-tube nanotubes are obtained (Fig. S4(d) in the ESM).

On the other hand, when electrospun nanofibers are presintered to 280 °C at a low heating rate of 1 °C·min$^{-1}$ in air, $F_c$ is smaller than $F_a$ (Fig. 1(d) and Fig. S3(b) in the ESM). The radial pyrolysis direction of electrospun nanofibers is from the inside to the outside, so hollow nanotubes form (Fig. S5(b) in the ESM) [50]. After the sample is held at 280 °C for 1 h, shrinkable nanotubes are also obtained (Fig. 1(e) and Fig. S5(c) in the ESM). The internal surface of the shrinkable nanotubes aggregates more inorganic salts, and the outer surface forms a relatively rigid shell. When the sample is heated to 500 °C at a high heating rate of 10 °C·min$^{-1}$, $F_c$ exceeds $F_a$ (Fig. 1(f)). The shrinkable nanotubes are split into tube-in-tube nanotubes from the center of the composite walls [6, 30]. Eventually, shrinkable tube-in-tube nanotubes are obtained (Fig. S5(d) in the ESM).

The shrinkable $CoMn_2O_4$ wire-in-tube and tube-in-tube nanotubes are both very uniform (Figs. 2(a) and 2(e)). TEM images clearly indicate the interior structures (Figs. 2(b), 2(c), 2(f), and 2(g)). The shrinkable wire-in-tube nanotubes consist of inner thin wires (~40 nm in diameter) and outer shrinkable tubes (~200 nm in diameter) (Figs. 2(b) and 2(c)). According to a statistical analysis, the diameters of different inner wires and outer tubes exhibit regular distributions, showing uniform diameters (Fig. S6 in the ESM). Further, the shrinkable tube-in-tube nanotubes are composed of shrinkable inner tubes (~110 nm in diameter, ~10 nm in wall thickness) and outer tubes (~200 nm in diameter, ~10 nm in wall thickness) (Figs. 2(g) and 2(f), and Fig. S7 in the ESM). High-resolution TEM (HRTEM) images indicate that these wire-in-tube and tube-in-tube architectures consist of uniform nanoparticles (~10 nm in diameter) (Figs. 2(d) and 2(h)). The corresponding selected-area electron diffraction (SAED) patterns indicate polycrystallinity (insets of Figs. 2(d) and 2(h)). The X-ray diffraction (XRD) patterns can be well indexed to pure $CoMn_2O_4$

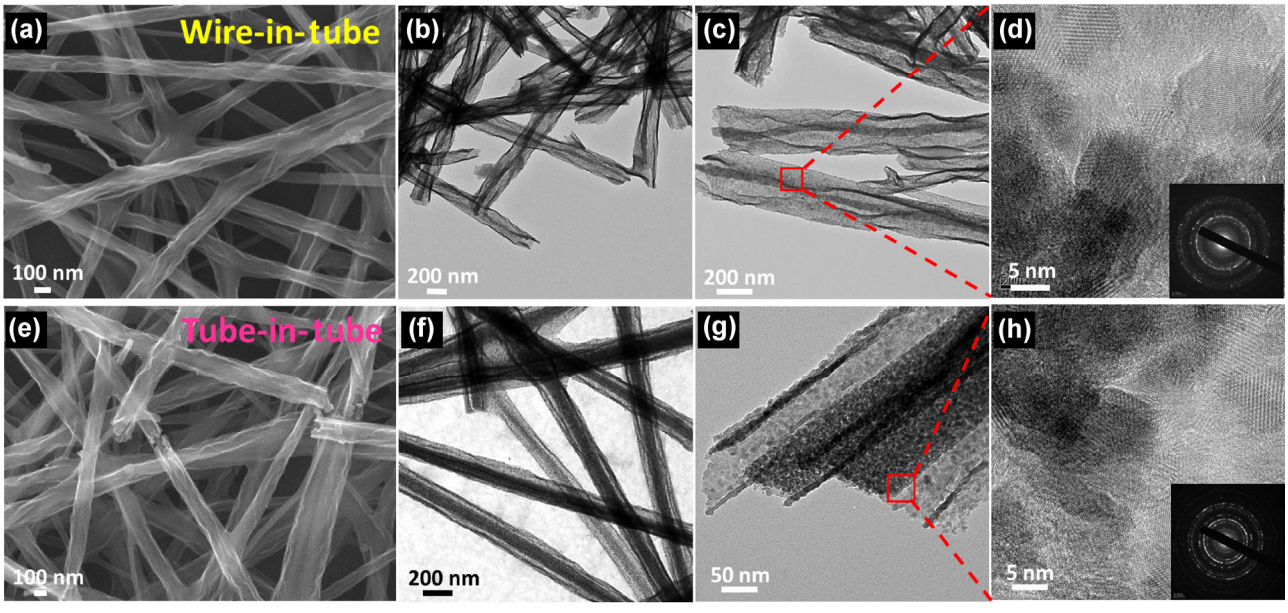


**Figure 2** SEM images ((a) and (e)), TEM images ((b), (c), (f), and (g)), HRTEM images ((d) and (h)), and SAED patterns (insets of (d) and (h)) of shrinkable $CoMn_2O_4$ wire-in-tube ((a)–(d)) and tube-in-tube ((e)–(h)) nanotubes.

phases (JCPDS card No. 01-077-0471) (Fig. S8 in the ESM). The carbon content of shrinkable $CoMn_2O_4$ tube-in-tube nanotubes was measured by TG measurement (Fig. S9(a) in the ESM), which showed that the carbon source was burned out after treatment at 500 °C in air. The nitrogen adsorption–desorption isotherm of the shrinkable $CoMn_2O_4$ tube-in-tube nanotubes shows a high BET specific surface area of 105.8 $m^2 \cdot g^{-1}$ (Fig. S9(b) in the ESM). The pore size distribution is mainly between 5 and 50 nm, indicating mesopores (Fig. S9(c) in the ESM). The mesopores are attributed to the random and loose stacking of nanocrystal grains, the sizes of which can also be tuned by modulating the compositions and concentrations of inorganic salts (Table S2 in the ESM).

### 3.2 General synthesis and wide applicability

To further confirm the versatility of our strategy, $MnCo_2O_4$ and $NiCo_2O_4$ shrinkable wire-in-tube and tube-in-tube nanotubes were also fabricated by adjusting the inorganic salts (Fig. 3). The broken terminals of these nanotubes clearly reveal the inner structures. The corresponding TEM images give more direct evidence for the wire-in-tube and tube-in-tube structures (Figs. 3(b), 3(d), 3(f), and 3(h)). The XRD patterns are well indexed to the pure phase of each sample (Fig. S10 in the ESM). Furthermore, our strategy can also be easily applied to the synthesis of shrinkable wire-in-tube and tube-in-tube nanotubes of various single metal oxides, such as $Co_3O_4$ and $MnO_2$ (Fig. S11 in the ESM). By using the XRD Rietveld refinement method, the average crystal size of shrinkable $Co_3O_4$ tube-in-tube nanotubes is found to be about 13.7 nm (Fig. S12 in the ESM), which is close to the value from HRTEM characterization. Overall, this strategy can be widely applied to synthesize shrinkable nanotubes with tunable interior structures for various metal oxides.

In our strategy, the application of different holding temperatures and heating rates is of great significance in the formation of shrinkable metal oxide nanotubes with tunable interior structures. Initially, the holding temperature plays an important role in shrinkage of the nanotubes. Simple $CoMn_2O_4$ nanotubes can be obtained without using different holding temperatures and heating rates, as reported in our previous work (Fig. S13 in the ESM) [50]. In contrast, when the nanofibers are treated only with different holding temperatures, shrinkable $CoMn_2O_4$ nanotubes are realized (Figs. 4(a) and 4(b)). In addition, different heating rates are crucial in obtaining multilevel nanotubes, including tube-in-tube nanotubes

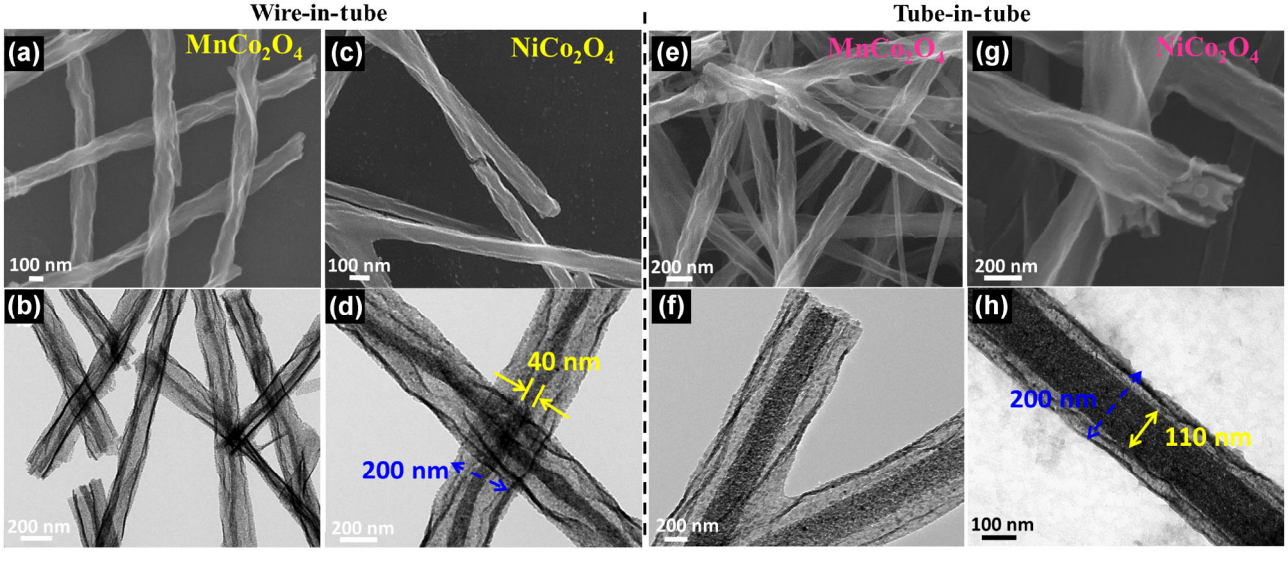


**Figure 3** (a) and (b) SEM and TEM images of shrinkable $MnCo_2O_4$ wire-in-tube nanotubes; (c) and (d) SEM and TEM images of shrinkable $NiCo_2O_4$ wire-in-tube nanotubes; (e) and (f) SEM and TEM images of shrinkable $MnCo_2O_4$ tube-in-tube nanotubes; (g) and (h) SEM and TEM images of shrinkable $NiCo_2O_4$ tube-in-tube nanotubes.

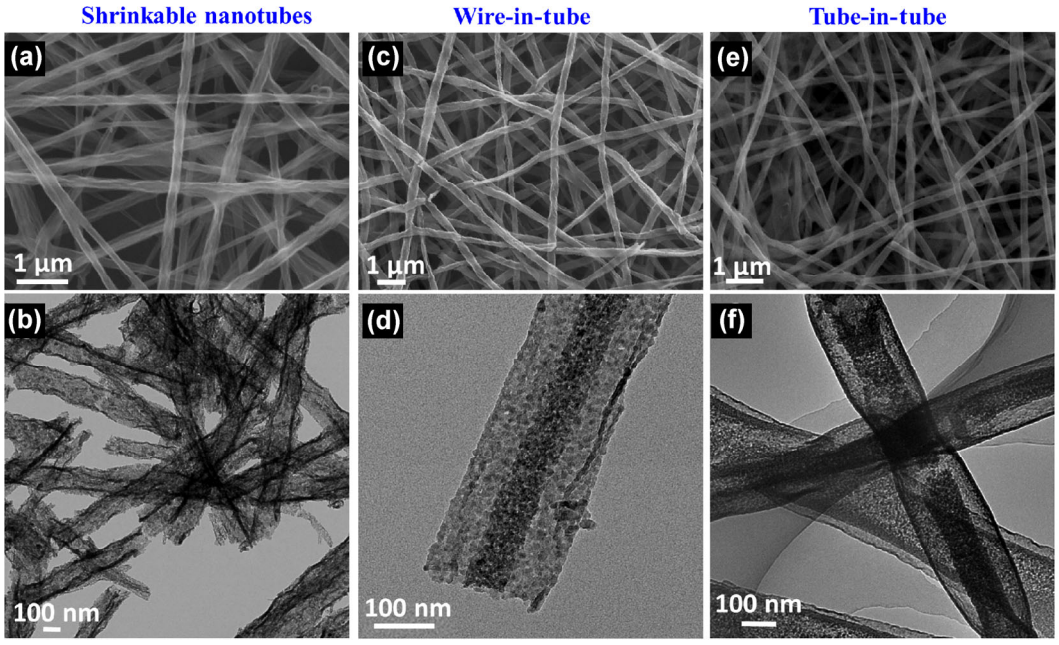


**Figure 4** ((a), (c), and (e)) SEM and ((b), (d), (f)) TEM images of ((a) and (b)) shrinkable $CoMn_2O_4$ nanotubes, ((c) and (d)) $CoMn_2O_4$ wire-in-tube nanotubes, and ((e) and (f)) $CoMn_2O_4$ tube-in-tube nanotubes.

and wire-in-tube nanotubes. When only different heating rates are applied, $CoMn_2O_4$ wire-in-tube nanotubes and tube-in-tube nanotubes are obtained (Figs. 4(c)–4(f)). In particular, by applying multistep heating rates, we can obtain multishelled nanotubes (Fig. S14 in the ESM). All the results demonstrate that this method of controlling the heat treatment is an efficient, general, and facile strategy for obtaining various nanotubes with tunable interior structures.

For the general synthesis of shrinkable metal oxide nanotubes with tunable interior structures, there are three prerequisites: (1) a large amount of inorganic salts, (2) electrospun nanofibers with relatively large diameter, and (3) a radial gradient of low-, medium-, and high-molecular-weight PVA. First, the concentration of metal salts determines whether robust metal oxide shells form. It is difficult for electrospun nanofibers with a low metal precursor concentration to form multilevel nanotubes. In addition, the peaks of the XRD patterns become wider with increasing concentration of metal salts (Table S2 in the ESM). The corresponding average crystallite sizes, which were obtained on the basis of the Scherrer formula, decrease slightly [52]. This can be attributed to the formation of more crystal nuclei at high concentrations. Second, during heat treatment, separation occurs between the metal oxide shells and the PVA/S composites owing to two opposite forces. In this separation, an effective distance is needed. Electrospun nanofibers with a smaller diameter tend to form single-shell nanotubes. Third, the radial gradient of low-, medium-, and high-molecular-weight PVA ensures that the pyrolysis direction of PVAs is from the inside to the outside along the radial direction, leading to the formation of nanotubes. In contrast, electrospun nanofibers with only medium-molecular-weight PVA cannot form these multilevel nanotubes under the same heat treatment process (Fig. S15 in the ESM). Thus, gradient electrospun nanofibers with a larger diameter and higher metal ion concentration may support the formation of 1D multilevel interior structures.

### 3.3 Electrochemical performance in LIB and ORR

First, electrochemical measurements of shrinkable $CoMn_2O_4$ tube-in-tube nanotubes used as anodes for an LIB were performed. As reported previously, another drawback of metal oxides is their low electronic conductivity [43]. To realize better use of their structural advantages, graphene oxides at a weight ratio of only 5% were used instead of the insulating binder,

which can enhance the electronic conductivity of the electrodes [44]. The CVs of the electrodes are characterized in the range from 0.01 to 3.0 V vs. $Li^+/Li$ at a scan rate of 0.2 $mV \cdot s^{-1}$ (Fig. 5(a)). Two pairs of distinct redox peaks in the curves correspond to the reduction/oxidation of both manganese oxides and cobalt oxides; the one at ~1.40 V is due to the oxidation of Mn to $Mn^{2+}$, and the one at ~2.00 V is due to the oxidation of Co to $Co^{2+}$, which is consistent with the previously reported results [23]. The second and third curves mostly overlap, showing good reversibility of the electrochemical reactions. Shrinkable $CoMn_2O_4$ tube-in-tube nanotubes can recover 90% of their initial capacity after testing at various current densities from 100 to 5,000 $mA \cdot g^{-1}$ (Fig. 5(b)). The average discharge specific capacities are 953, 917, 854, 781, 666, and 452 $mAh \cdot g^{-1}$ at 100, 200, 500, 1,000, 2,000, and 5,000 $mA \cdot g^{-1}$, respectively. The corresponding charge–discharge voltage profiles of the rate performance exhibit low polarization and high Coulombic efficiency (Fig. 5(c)). In addition, after cycling 140 times at 200 $mA \cdot g^{-1}$, the battery can maintain a discharge capacity of 923 $mAh \cdot g^{-1}$ with a capacity retention of 98% compared with the capacity of the second cycle (Fig. 5(d)). In particular, even measured at the high rate of 2 $A \cdot g^{-1}$, shrinkable $CoMn_2O_4$ tube-in-tube nanotubes can still remain stable after 500 cycles, with a capacity retention of 89% and a tiny capacity fading of 0.44% per cycle (Fig. 5(e)). Compared with other nanostructured $CoMn_2O_4$ in previous reports, our synthesized shrinkable $CoMn_2O_4$ tube-in-tube nanotubes possess outstanding high-rate and long-life cycling performance (Table S3 in the ESM).

To further reveal their structural superiority, shrinkable $CoMn_2O_4$ tube-in-tube nanotubes were also characterized for the ORR. First, the electrocatalytic activities of VXC72R, Pt/C, and $CoMn_2O_4$ nanotubes were evaluated in terms of their CVs (Fig. 6(a)). A well-defined cathodic peak appears at ~0.81 V, which is close to that of Pt/C (0.86 V) and more positive than that of VXC72R (0.67 V). From the LSV curves in rotating disk electrode (RDE) experiments at 1,600 rpm, the onset potential of the $CoMn_2O_4$ nanotubes is ~0.9 V, which is consistent with that identified from CV measurement (Fig. 6(b)). Additionally, a clear plateau in the diffusion-limiting current of the $CoMn_2O_4$ nano-

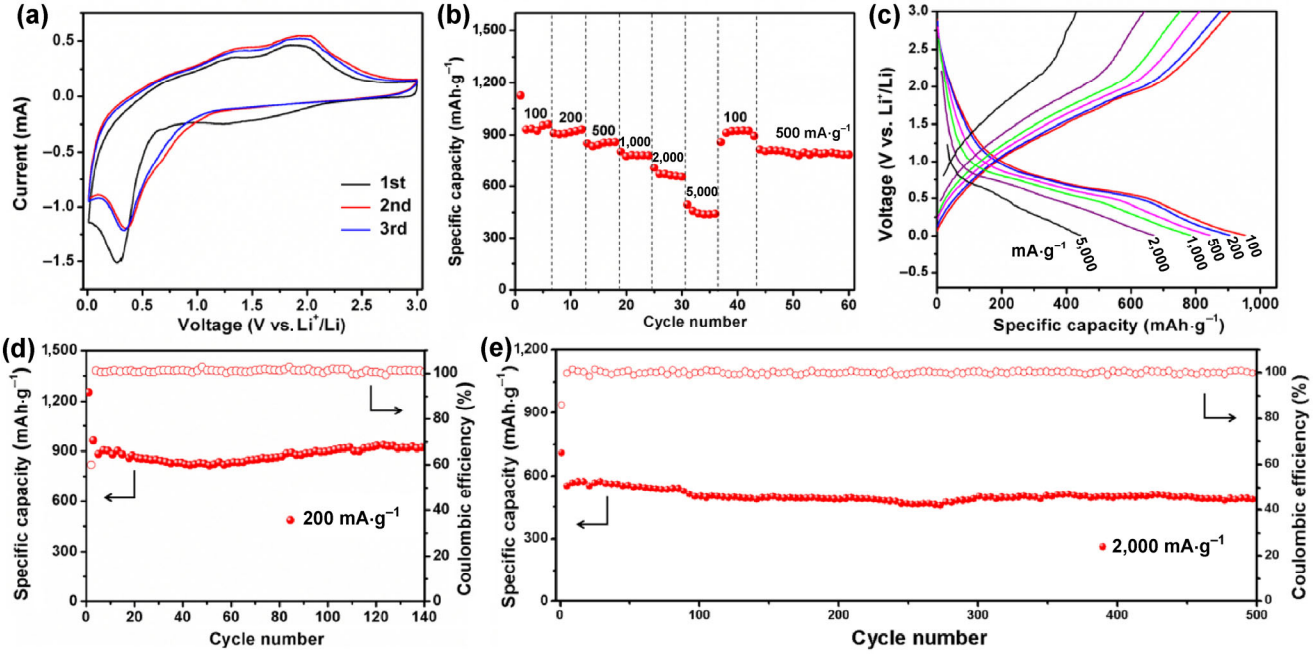


**Figure 5** Electrochemical performance of shrinkable $CoMn_2O_4$ tube-in-tube nanotubes in LIB. (a) First three CV curves tested at a scan rate of 0.2 $mV \cdot s^{-1}$ in a potential range from 0.01 to 3.0 V vs. $Li^+/Li$. (b) Rate performance tested at current densities of 100, 200, 500, 1,000, 2,000, and 5,000 $mA \cdot g^{-1}$. (c) Corresponding charge–discharge voltage profiles. ((d) and (e)) Cycling performance and Coulombic efficiency tested at current densities of 200 and 2,000 $mA \cdot g^{-1}$, respectively.

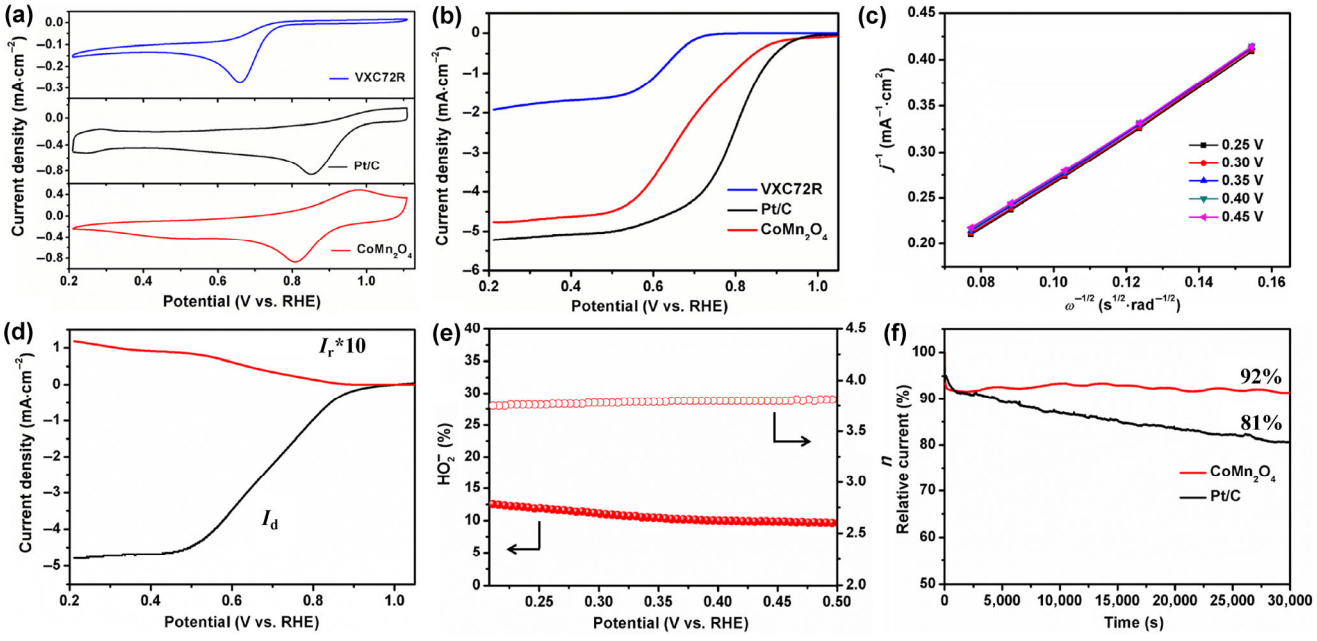


**Figure 6** Electrochemical ORR of shrinkable $CoMn_2O_4$ tube-in-tube nanotubes. (a) CV curves of VXC72R, Pt/C, and $CoMn_2O_4$ nanotubes in $O_2$-saturated 0.1 M KOH at a scan rate of 5 mV·s$^{-1}$. (b) LSV curves of VXC72R, Pt/C, and $CoMn_2O_4$ nanotubes in $O_2$-saturated 0.1 M KOH at 5 mV·s$^{-1}$ and 1,600 rpm. (c) K–L plots of $CoMn_2O_4$ nanotubes at different potentials. (d) RRDE voltammograms recorded with $CoMn_2O_4$ nanotubes in $O_2$-saturated 0.1 M KOH at 1,600 rpm. (e) Peroxide yields and electron transfer numbers of $CoMn_2O_4$ nanotubes at various potentials based on RRDE data. (f) Current–time chronoamperometric responses of $CoMn_2O_4$ nanotubes and Pt/C in $O_2$-saturated 0.1 M KOH at 0.65 V and 1,225 rpm.

tubes is observed, indicating that a stable ORR process can be achieved owing to the strong electrocatalytic activity. RDE experiments at different rotation rates were performed (Fig. S16 in the ESM), and the corresponding kinetic parameters were analyzed using the K–L equation (Fig. 6(c)). The linearity of the K–L plots indicates the first-order reaction kinetics with regard to the concentration of dissolved oxygen and similar electron transfer numbers at various potentials [53]. The value of $n$ below 0.5 V is 3.6, suggesting an apparent quasi-4e$^-$ ORR pathway. Moreover, the ORR catalytic behaviors were evaluated in terms of the transferred electron numbers ($n$) and yield of peroxide species from the disk and ring currents recorded on the RRDEs (Fig. 6(d)). The $HO_2^-$ yield for the $CoMn_2O_4$ nanotubes is less than 13%, and the calculated electron transfer number is 3.75, which is close to the results obtained from the K–L plots based on RDE measurement. Furthermore, the chronoamperometric responses were measured to evaluate the durability of $CoMn_2O_4$ nanotubes and Pt/C at 0.65 V and 1,225 rpm. The $CoMn_2O_4$ nanotubes exhibited excellent stability with 92% current retention after 30,000 s, which is much better than the value for Pt/C (81%).

The excellent lithium storage and electrocatalytic properties of shrinkable nanotubes with tunable interior structures can be attributed to the following factors (Fig. 7 and Fig. S17 in the ESM). First, for LIBs (Fig. 7(a)), such a structure can give rise to a high BET specific surface area of 105.8 m$^2$·g$^{-1}$. This architecture can enhance the electrode/electrolyte contact surface and shorten the path length for ionic and electronic transport [54]. Second, the hollow interior spaces and mesopores can efficiently accommodate large volume variation and strain during the $Li^+$ insertion/removal process. Further, the morphology can remain integrated after long cycles, showing great structural stability (Fig. S18 in the ESM). In addition, the packing density of shrinkable tube-in-tube nanotubes can be increased by 26.3% compared to that of unshrinkable tube-in-tube nanotubes, which efficiently enhances the volumetric energy and power densities (Fig. S19 in the ESM). Electrochemical impedance spectroscopy measurement was performed (Fig. S20 in the ESM).

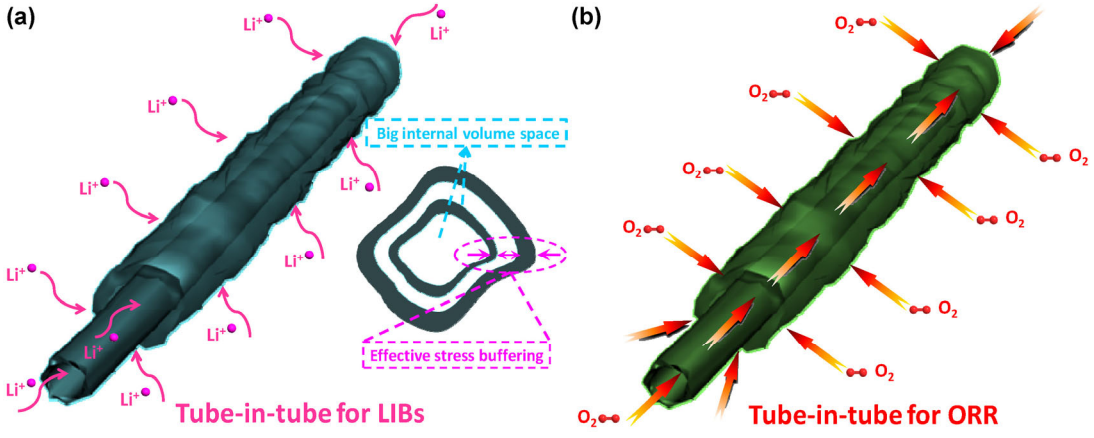


**Figure 7** (a) Schematic illustration of shrinkable tube-in-tube nanotubes with effective stress buffering and enhanced $Li^+$ diffusion in LIB; (b) schematic illustration of shrinkable tube-in-tube nanotubes with efficient $O_2$ diffusion and fast mass transport in ORR.

The charge transfer resistance ($R_{ct}$) of electrodes based on shrinkable $CoMn_2O_4$ tube-in-tube nanotubes is 90 Ω, suggesting their fast electronic mobility. For ORR (Fig. 7(b)), the high surface area and multilevel mesoporous tubes are also beneficial because they provide more reaction active sites and enhanced mass transport during electrochemical reactions [55].

## 4 Conclusions

In this work, we demonstrate a facile and general interface-modulated method of synthesizing multilevel metal oxide nanotubes with tunable interior structures. By controlling the polymer/metal oxide interface, shrinkable wire-in-tube and tube-in-tube nanotubes are obtained. Further, this versatile strategy can be applied to synthesize various metal oxides. These metal oxide multilevel nanotubes provide more active reaction sites, faster mass transport, better strain accommodation, and higher packing density, which are advantageous for use in LIBs and the ORR. Specifically, when used as a lithium battery anode or an ORR catalyst, shrinkable $CoMn_2O_4$ tube-in-tube nanotubes exhibit both excellent electrochemical activity and stability. This general strategy marks a milestone in the design and synthesis of complex multilevel nanotubes.

## Acknowledgements

This work was supported by the National Basic Research Program of China (Nos. 2013CB934103 and 2012CB933003), the National Natural Science Foundation of China (Nos. 51521001 and 51272197), the National Science Fund for Distinguished Young Scholars (No. 51425204), the Hubei Province Natural Science Fund for Distinguished Young Scholars (No. 2014CFA035), and the Fundamental Research Funds for the Central Universities (Nos. 2015-III-032, 2016-YB-004, and 2015-KF-3). We thank Prof. D. Y. Zhao of Fudan University and Prof. J. Liu of Pacific Northwest National Laboratory for useful discussions and assistance with the manuscript.

**Electronic Supplementary Material:** Supplementary Material (TG curves, viscosity and average molecular weight of different PVAs; SEM images of composite nanowires after electrospinning; SEM images of the formation process of shrinkable $CoMn_2O_4$ tube-in-tube and tube-in-tube nanotubes; XRD patterns, diameter distributions, nitrogen adsorption–desorption isotherms and corresponding pore size distribution, LSV curves and AC impedance plot of shrinkable $CoMn_2O_4$ tube-in-tube nanotubes; SEM and TEM images of $CoMn_2O_4$ nanotubes and multishelled nanotubes; Crystalline sizes of shrinkable $Co_3O_4$ wire-in-tube nanotubes with different concentration; SEM images after cycling; SEM images and XRD patterns of shrinkable $Co_3O_4$ and $MnO_2$ wire-in-tube and tube-in-tube nanotubes) is available in the online version of this article at http://dx.doi.org/10.1007/s12274-016-1130-x.

## References


[1] Jiang, H.; Hu, Y. J.; Guo, S. J.; Yan, C. Y.; Lee, P. S.; Li, C. Z. Rational design of MnO/carbon nanopeapods with internal void space for high-rate and long-life Li-ion batteries. *ACS Nano* **2014**, *8*, 6038–6046.

[2] Li, J.; Tang, S. B.; Lu, L.; Zeng, H. C. Preparation of nano-composites of metals, metal oxides, and carbon nanotubes via self-assembly. *J. Am. Chem. Soc.* **2007**, *129*, 9401–9409.

[3] Wang, J.; Zhong, H. X.; Wang, Z. L.; Meng, F. L.; Zhang, X. B. Integrated three-dimensional carbon paper/carbon tubes/cobalt-sulfide sheets as an efficient electrode for overall water splitting. *ACS Nano* **2016**, *10*, 2342–2348.

[4] Wang, J.; Li, K.; Zhong, H. X.; Xu, D.; Wang, Z. L.; Jiang, Z.; Wu, Z. J.; Zhang, X. B. Synergistic effect between metal–nitrogen–carbon sheets and NiO nanoparticles for enhanced electrochemical water-oxidation performance. *Angew. Chem., Int. Ed.* **2015**, *54*, 10530–10534.

[5] Hu, L. B.; Chen, W.; Xie, X.; Liu, N.; Yang, Y.; Wu, H.; Yao, Y.; Pasta, M.; Alshareef, H. N.; Cui, Y. Symmetrical $MnO_2$-carbon nanotube-textile nanostructures for wearable pseudocapacitors with high mass loading. *ACS Nano* **2011**, *5*, 8904–8913.

[6] Mou, F. Z.; Guan, J. G.; Shi, W. D.; Sun, Z. G.; Wang, S. H. Oriented contraction: A facile nonequilibrium heat-treatment approach for fabrication of maghemite fiber-in-tube and tube-in-tube nanostructures. *Langmuir* **2010**, *26*, 15580–15585.

[7] Yu, W. J.; Liu, C.; Hou, P. X.; Zhang, L. L.; Shan, X. Y.; Li, F.; Cheng, H. M. Lithiation of silicon nanoparticles confined in carbon nanotubes. *ACS Nano* **2015**, *9*, 5063–5071.

[8] Yuan, C. Z.; Wu, H. B.; Xie, Y.; Lou, X. W. Mixed transition-metal oxides: Design, synthesis, and energy-related applications. *Angew. Chem., Int. Ed.* **2014**, *53*, 1488–1504.

[9] Wang, Y. X.; Yang, J. P.; Chou, S. L.; Liu, H. K.; Zhang, W. X.; Zhao, D. Y.; Dou, S. X. Uniform yolk-shell iron sulfide-carbon nanospheres for superior sodium-iron sulfide batteries. *Nat. Commun.* **2015**, *6*, 8689.

[10] Wang, Z. L.; Xu, D.; Xu, J. J.; Zhang, X. B. Oxygen electrocatalysts in metal-air batteries: From aqueous to nonaqueous electrolytes. *Chem. Soc. Rev.* **2014**, *43*, 7746–7786.

[11] Gao, Z.; Song, N. N.; Zhang, Y. Y.; Li, X. D. Cotton-textile-enabled, flexible lithium-ion batteries with enhanced capacity and extended lifespan. *Nano Lett.* **2015**, *15*, 8194–8203.

[12] Niu, C. J.; Meng, J. S.; Han, C. H.; Zhao, K. N.;Yan, M. Y.; Mai, L. Q. $VO_2$ nanowires assembled into hollow microspheres for high-rate and long-life lithium batteries. *Nano Lett.* **2014**, *14*, 2873–2878.

[13] Zhao, Y.; Jiang, L. Hollow micro/nanomaterials with multilevel interior structures. *Adv. Mater.* **2009**, *21*, 3621–3638.

[14] Fang, Y.; Zheng, G. F.; Yang, J. P.; Tang, H. S.; Zhang, Y. F.; Kong, B.; Lv, Y. Y.; Xu, C. J.; Asiri, A. M.; Zi, J. et al. Dual-pore mesoporous carbon@silica composite core–shell nanospheres for multidrug delivery. *Angew. Chem., Int. Ed.* **2014**, *53*, 5366–5370.

[15] Lai, X. Y.; Li, J.; Korgel, B. A.; Dong, Z. H.; Li, Z. M.; Su, F. B.; Du, J.; Wang, D. General synthesis and gas-sensing properties of multiple-shell metal oxide hollow microspheres. *Angew. Chem., Int. Ed.* **2011**, *50*, 2738–2741.

[16] Shao, M. F.; Ning, F. Y.; Zhao, Y. F.; Zhao, J. W.; Wei, M.; Evans, D. G.; Duan, X. Core–shell layered double hydroxide microspheres with tunable interior architecture for super-capacitors. *Chem. Mater.* **2012**, *24*, 1192–1197.

[17] Wu, J.; Wang, N.; Zhao, Y.; Jiang, L. Electrospinning of multilevel structured functional micro-/nanofibers and their applications. *J. Mater. Chem. A* **2013**, *1*, 7290–7305.

[18] Zhang, G. Q.; Lou, X. W. General synthesis of multi-shelled mixed metal oxide hollow spheres with superior lithium storage properties. *Angew. Chem., Int. Ed.* **2014**, *53*, 9041–9044.

[19] Zhu, Y. F.; Shi, J. L.; Shen, W. H.; Dong, X. P.; Feng, J. W.; Ruan, M. L.; Li, Y. S. Stimuli-responsive controlled drug release from a hollow mesoporous silica sphere/polyelectrolyte multilayer core-shell structure. *Angew. Chem., Int. Ed.* **2005**, *44*, 5083–5087.

[20] Lou, X. W.; Li, C. M.; Archer, L. A. Designed synthesis of coaxial $SnO_2$@carbon hollow nanospheres for highly reversible lithium storage. *Adv. Mater.* **2009**, *21*, 2536–2539.

[21] Lou, X. W.; Yuan, C.; Archer, L. A. Double-walled $SnO_2$ nano-cocoons with movable magnetic cores. *Adv. Mater.* **2007**, *19*, 3328–3332.

[22] Dong, Z. H.; Lai, X. Y.; Halpert, J. E.; Yang, N. L.; Yi, L. X.; Zhai, J.; Wang, D.; Tang, Z. Y.; Jiang, L. Accurate control of multishelled ZnO hollow microspheres for dye-sensitized solar cells with high efficiency. *Adv. Mater.* **2012**, *24*, 1046–1049.

[23] Zhou, L.; Zhao, D. Y.; Lou, X. W. Double-shelled $CoMn_2O_4$ hollow microcubes as high-capacity anodes for lithium-ion batteries. *Adv. Mater.* **2012**, *24*, 745–748.

[24] Aravindan, V.; Sundaramurthy, J.; Kumar, P. S.; Lee, Y. S.; Ramakrishna, S.; Madhavi, S. Electrospun nanofibers: A prospective electro-active material for constructing high performance Li-ion batteries. *Chem. Commun.* **2015**, *51*, 2225–2234.

[25] Sun, Y. G.; Mayers, B.; Xia, Y. N. Metal nanostructures with hollow interiors. *Adv. Mater.* **2003**, *15*, 641–646.

[26] Wang, H. G.; Yuan, S.; Ma, D. L.; Zhang, X. B.; Yan, J. M. Electrospun materials for lithium and sodium rechargeable batteries: From structure evolution to electrochemical performance. *Energy Environ. Sci.* **2015**, *8*, 1660–1681.

[27] Xia, Y. N.; Yang, P. D.; Sun, Y. G.; Wu, Y. Y.; Mayers, B.; Gates, B.; Yin, Y. D.; Kim, F.; Yan, H. Q. One-dimensional nanostructures: Synthesis, characterization, and applications. *Adv. Mater.* **2003**, *15*, 353–389.

[28] Yu, Y.; Gu, L.; Wang, C. L.; Dhanabalan, A.; Van Aken, P. A.; Maier, J. encapsulation of Sn@carbon nanoparticles in bamboo-like hollow carbon nanofibers as an anode material in lithium-based batteries. *Angew. Chem., Int. Ed.* **2009**, *48*, 6485–6489.

[29] Luo, W.; Lorger, S.; Wang, B.; Bommier, C.; Ji, X. L. Facile synthesis of one-dimensional peapod-like Sb@C submicron-structures. *Chem. Commun.* **2014**, *50*, 5435–5437.

[30] Peng, S. J.; Li, L. L.; Hu, Y. X.; Srinivasan, M.; Cheng, F. Y.; Chen, J.; Ramakrishna, S. Fabrication of spinel one-dimensional architectures by single-spinneret electrospinning for energy storage applications. *ACS Nano* **2015**, *9*, 1945–1954.

[31] Xu, J. J.; Xu, D.; Wang, Z. L.; Wang, H. G.; Zhang, L. L.; Zhang, X. B. Synthesis of perovskite-based porous $La_{0.75}Sr_{0.25}MnO_3$ nanotubes as a highly efficient electro-catalyst for rechargeable lithium-oxygen batteries. *Angew. Chem., Int. Ed.* **2013**, *52*, 3887–3890.

[32] Zhang, G. Q.; Xia, B. Y.; Xiao, C.; Yu, L.; Wang, X.; Xie, Y.; Lou, X. W. General formation of complex tubular nanostructures of metal oxides for the oxygen reduction reaction and lithium-ion batteries. *Angew. Chem., Int. Ed.* **2013**, *52*, 8643–8647.

[33] Cai, Z. Y.; Xu, L.; Yan, M. Y.; Han, C. H.; He, L.; Hercule, K. M.; Niu, C. J.; Yuan, Z. F.; Xu, W. W.; Qu, L. B. et al. Manganese oxide/carbon yolk-shell nanorod anodes for high capacity lithium batteries. *Nano Lett.* **2015**, *15*, 738–744.

[34] Zhang, Z. T.; Guo, K. P.; Li, Y. M.; Li, X. Y.; Guan, G. Z.; Li, H. P.; Luo, Y. F.; Zhao, F. Y.; Zhang, Q.; Wei, B. et al. A colour-tunable, weavable fibre-shaped polymer light-emitting electrochemical cell. *Nat. Photonics* **2015**, *9*, 233–238.

[35] Meng, J. S.; Liu, Z. A.; Niu, C. J.; Xu, X. M.; Liu, X.; Zhang, G. B.; Wang, X. P.; Huang, M.; Yu, Y.; Mai, L. Q. A synergistic effect between layer surface configurations and K ions of potassium vanadate nanowires for enhanced energy storage performance. *J. Mater. Chem. A* **2016**, *4*, 4893–4899.

[36] Hu, Y. X.; Zhang, T. R.; Cheng, F. Y.; Zhao, Q.; Han, X. P.; Chen, J. Recycling application of Li-$MnO_2$ batteries as rechargeable lithium-air batteries. *Angew. Chem., Int. Ed.* **2015**, *54*, 4338–4343.

[37] Lang, X. Y.; Hirata, A.; Fujita, T.; Chen, M. W. Nanoporous metal/oxide hybrid electrodes for electrochemical super-capacitors. *Nat. Nanotechnol.* **2011**, *6*, 232–236.

[38] Huang, X. L.; Wang, R. Z.; Xu, D.; Wang, Z. L.; Wang, H. G.; Xu, J. J.; Wu, Z.; Liu, Q. C.; Zhang, Y.; Zhang, X. B. Homogeneous CoO on graphene for binder-free and ultralong-life lithium ion batteries. *Adv. Funct. Mater.* **2013**, *23*, 4345–4353.

[39] Mai, L. Q.; Tian, X. C.; Xu, X.; Chang, L.; Xu, L. Nanowire electrodes for electrochemical energy storage devices. *Chem. Rev.* **2014**, *114*, 11828–11862.

[40] Ren, Y.; Ma, Z.; Bruce, P. G. Ordered mesoporous metal oxides: Synthesis and applications. *Chem. Soc. Rev.* **2012**, *41*, 4909–4927.

[41] Huang, X. L.; Xu, D.; Yuan, S.; Ma, D. L.; Wang, S.; Zheng, H. Y.; Zhang, X. B. Dendritic Ni-P-coated melamine foam for a lightweight, low-cost, and amphipathic three-dimensional current collector for binder-free electrodes. *Adv. Mater.* **2014**, *26*, 7264–7270.

[42] Zhao, K. N.; Liu, F. N.; Niu, C. J.; Xu, W. W.; Dong, Y. F.; Zhang, L.; Xie, S. M.;Yan, M. Y.; Wei, Q. L.; Zhao, D. Y. et al. Graphene oxide wrapped amorphous copper vanadium oxide with enhanced capacitive behavior for high-rate and long-life lithium-ion battery anodes. *Adv. Sci.* **2015**, *2*, 1500154.

[43] Palacin, M. R. Recent advances in rechargeable battery materials: A chemist's perspective. *Chem. Soc. Rev.* **2009**, *38*, 2565–2575.

[44] Yu, D. S.; Goh, K.; Wang, H.; Wei, L.; Jiang, W. C.; Zhang, Q.; Dai, L. M.; Chen, Y. Scalable synthesis of hierarchically structured carbon nanotube-graphene fibres for capacitive energy storage. *Nat. Nanotechnol.* **2014**, *9*, 555–562.

[45] Yang, X. W.; Cheng, C.; Wang, Y. F.; Qiu, L.; Li, D. Liquid-mediated dense integration of graphene materials for compact capacitive energy storage. *Science* **2013**, *341*, 534–537.

[46] Li, C.; Han, X. P.; Cheng, F. Y.; Hu, Y. X.; Chen, C. C.; Chen, J. Phase and composition controllable synthesis of cobalt manganese spinel nanoparticles towards efficient oxygen electrocatalysis. *Nat. Commun.* **2015**, *6*, 7345.

[47] Liang, Y. Y.; Wang, H. L.; Zhou, J. G.; Li, Y. G.; Wang, J.; Regier, T.; Dai, H. J. Covalent hybrid of spinel manganese-cobalt oxide and graphene as advanced oxygen reduction

electrocatalysts. *J. Am. Chem. Soc.* **2012**, *134*, 3517–3523.

[48] Menezes, P. W.; Indra, A.; Sahraie, N. R.; Bergmann, A.; Strasser, P.; Driess, M. Cobalt-manganese-based spinels as multifunctional materials that unify catalytic water oxidation and oxygen reduction reactions. *ChemSusChem* **2015**, *8*, 164–171.

[49] Zhang, T. R.; Cheng, F. Y.; Du, J.; Hu, Y. X.; Chen, J. Efficiently enhancing oxygen reduction electrocatalytic activity of $MnO_2$ using facile hydrogenation. *Adv. Energy Mater.* **2015**, *5*, 1400654.

[50] Niu, C. J.; Meng, J. S.; Wang, X. P.; Han, C. H.; Yan, M. Y.; Zhao, K. N.; Xu, X. M.; Ren, W. H.; Zhao, Y. L.; Xu, L. et al. General synthesis of complex nanotubes by gradient electrospinning and controlled pyrolysis. *Nat. Commun.* **2015**, *6*, 7402.

[51] Liang, J.; Yu, X. Y.; Zhou, H.; Wu, H. B.; Ding, S. J.; Lou, X. W. Bowl-like $SnO_2$@carbon hollow particles as an advanced anode material for lithium-ion batteries. *Angew. Chem., Int. Ed.* **2014**, *53*, 12803–12807.

[52] Sciacca, B.; Yalcin, A. O.; Garnett, E. C. Transformation of Ag nanowires into semiconducting $AgFeS_2$ nanowires. *J. Am. Chem. Soc.* **2015**, *137*, 4340–4343.

[53] Zhang, H. X.; Wang, J.; Zhang, Y. W.; Xu, W. L.; Xing, W.; Xu, D.; Zhang, Y. F.; Zhang, X. B. ZIF-8 derived graphene-based nitrogen-doped porous carbon sheets as highly efficient and durable oxygen reduction electrocatalysts. *Angew. Chem., Int. Ed.* **2014**, *53*, 14235–14239.

[54] Wang, Z. L.; Xu, D.; Wang, H. G.; Wu, Z.; Zhang, X. B. *In situ* fabrication of porous graphene electrodes for high-performance energy storage. *ACS Nano* **2013**, *7*, 2422–2430.

[55] Xia, B. Y.; Yan, Y.; Li, N.; Wu, H. B.; Lou, X. W.; Wang, X. A metal–organic framework-derived bifunctional oxygen electrocatalyst. *Nat. Energy* **2016**, *1*, 15006.